BEN LI[1], SHANJUN MAO[1*], HAOYUAN ZHANG[1],
XINCHAO LI[2], HUAZHOU CHEN[2]

AUTOMATED REAL-TIME ABSOLUTE POSITIONING TECHNOLOGY ON INTELLIGENT FULLY MECHANISED COAL FACES USING THE GYRO RTS SYSTEM

The absolute positions of shearers on advancing coal faces are requisite for providing references for adaptive mining combined with geological models. Common coalmine localization techniques (e.g. UWB, INS, etc.) are not fully applicable to adaptive mining due to their drifting error or the messy environment. The gyro robotic total station (RTS) is versatile and precise in measuring coordinates in coal mines, while its conventional usage is of low automation and poor timeliness, impeding its application on mining faces. This article proposed an automated gyro RTS system for real-time absolute positioning on fully mechanised coal faces. The measuring process was changed to fit mining requirements, and a new state-transferring model was used to automate it. Programs were developed and installed in available instruments, forming a prototype. Field experiments were carried out on a simulative working face, verifying the system's accuracy and applicability. Results show that the relative positioning error is better than 2.6143×10^{-4}, which meets the demand of advancing faces. The error of the gyro is estimated at 55.5187", justifying its nominal indicators. To sum up, the automated gyro RTS system proposed in this paper can offer real-time and accurate absolute positions of equipment on working faces, supporting adaptive mining combined with the geological model.

Keywords: Fully mechanised faces; absolute positioning; adaptive mining; gyro RTS; automated measuring

1. Introduction

With the development of manufacturing and information technology, mining coal has become increasingly automated [1] and intelligent [2-4]. Many key technologies (e.g. high-precision

1   PEKING UNIVERSITY, INSTITUTE OF REMOTE SENSING AND GEOGRAPHIC INFORMATION SYSTEM, BEIJING 100871, CHINA
2   BEIJING LONGRUAN TECHNOLOGIES CO., LTD., BEIJING 100871, CHINA

*   Corresponding author: sjmao_@pku.edu.cn

geological model, TGIS platform, geological database, etc.) have been studied and applied to coal mines successfully, making substantial progress in intelligent mining [5-8]. To achieve intelligent coal mining, one of the basic technologies is positioning equipment, especially on advancing faces. For example, the shearer continuously moves along the coal face and cuts coal seams, and its accurate dynamic positions can form the mining trajectories. These are necessary references to analyse mining safety and efficiency [9]. By analysing the trajectories and mechanical dimension parameters, the cutting lines and face straightness can be determined. Referring to the established geographical model, future mining paths and conveyor lines can be optimally adjusted, which is conducive to adaptive mining.

Many methods of equipment positioning in underground coal mines have been studied, such as the wireless sensors network (WSN), the inertial navigation system (INS), radars, laser scanners, computer vision methods, etc. WSN is one of the most widely-used for localisation in GNSS-free space [10]. The sensors are deployed on spots of interest and communicate with each other by wireless radio [11,12]. Types of positioning algorithms include geometric methods, proximity methods and fingerprint recognition. However, it suffers from a major limitation in that its positioning accuracy (i.e. metre level) and connective stability are insufficient for providing reliable positions of equipment on advancing face. The INS measures the three-axis linear acceleration and angular velocity of its carrier and then obtains the displacement by coordinate frame transformation and the double integration of acceleration [13]. The Kalman filter and its variants are usually used to improve positioning accuracy. However, the main problem of INS is the accumulated drifting error, so it has to be combined with odometry and always needs to be calibrated. The radars can be used to localise equipment [14] but only in one dimension. So that 3D coordinates of the equipment cannot be obtained. At last, the laser scanner [15] and computer vision [16] are effective tools for simultaneous localisation and mapping (SLAM). The LiDAR can be used to detect hydraulic supports and aids the INS to position the longwall shearer [17]. Machine vision is used in the real-time measuring of roadway deformation [18]. However, they are inapplicable in the changing scenario (e.g. the advancing coal face) and are inconvenient for absolute positioning.

The robotic total station (RTS) is a sort of specialised surveying instrument, which directly measures the distances and the angles of targets even kilometres away and then calculates corresponding accurate 3D coordinates. With the servomotor, the automated target recognition (ATR) and the powerful search functions, an RTS can search, track and measure targets mechanically. Due to its high accuracy and versatility, the RTS can be used not only in conventional surveying, but even for monitoring the deformation of tunnels [19,20], dams [21], and bridges [22,23]. In addition, if the RTS is equipped with a gyroscope, it will be able to orient itself, reducing dependency on control points and extending its applicability. In terms of measuring precision, the highly precise gyro RTS can even meet the demand of first-order astronomical azimuths [24] and can be used to establish the baseline field [25]. As a result, the gyro RTS shows its outstanding advantages in scenarios that lack reference information. In tunnel projects, the gyro RTS provides high-accuracy azimuth measuring from the perspective of transfixion measurement [26]. In coal mine projects, the gyro RTS can save labour and relieve difficulties of shaft deepening and connection measuring by reducing dependency on control points [27,28]. The RTS is accurate to the millimetre, which far exceeds WSN methods. Each position measurement is independent of the other, so it avoids accumulating errors like the INS. Compared with positioning methods of LiDAR and machine vision, the RTS can be more accurate and applicable. The conventional usage of the gyro RTS is a manual operation, which includes levelling, centring, aiming and mov-

ing station. However, positioning equipment on an advancing coal face in this way causes high personnel risk and low efficiency. In addition, it's difficult to achieve real-time mining support when using manually measured results since they can't be uploaded promptly.

Aiming to achieve real-time accurate absolute positioning and coordinates transmission on dynamic fully mechanised faces, this paper proposes an automated gyro RTS measuring system. In section I, the problems of positioning on adaptive mining face are raised and the related background is introduced. In section II, we introduce the measuring process, the state-transferring model and the error model used by the automated gyro RTS system. In section III, the prototype is introduced, formed by developed programs and available instruments. In section IV, field experiments were carried out, and corresponding results are shown to verify the accuracy and applicability of the system. More details about error characteristics are discussed in section V, especially on the precision estimation of the gyroscope. Finally, summaries and conclusions are drawn in section VI.

2. Theoretical model

2.1. The measuring process of gyro RTS

The outstanding feature of the gyro RTS is its capability to orient itself (i.e. aligning its horizontal zero direction to the local true north). The gyro RTS has an indicator called the gyro bias. After the orientation is completed and the bias is compensated, the coordinate framework of RTS is parallel to the geodetic coordinate framework. Then the difference between the geodetic coordinates and the Gauss-Kruger coordinates should be considered because the commonly used coordinate framework in coal mines is the G-K projection grid. As for any point in a G-K projection zone, its local true north is tangential to its local meridian, while its grid north is parallel to the central meridian in its zone. The differential angle between its local north and grid north defines the convergence of meridians γ.
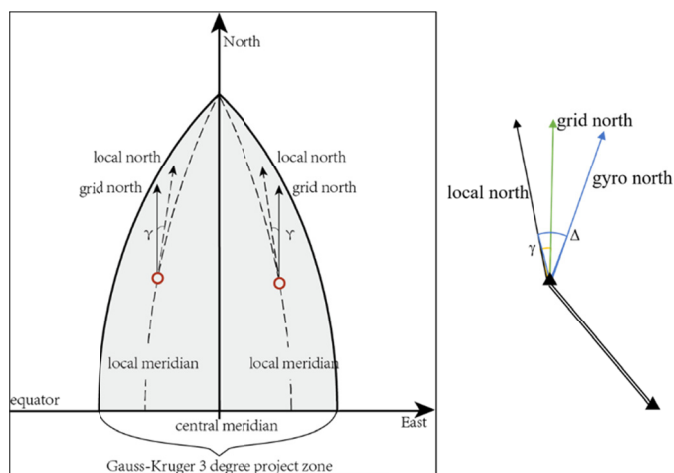
Fig. 1. The convergence of meridians and the relationship between grid north, local north and gyro north

478

Fig. 1, γ denotes the convergence of meridians and Δ denotes the gyro bias. To ensure the gyro RTS measures the G-K coordinates, the bias should be compensated and the convergence of meridians should be corrected. Furthermore, Δ is determined by datum points on the ground, while γ is calculated by Eq. (1):

$$\gamma = \left(L_{\text{local}} - L_{\text{cen}}\right) \times \sin B \tag{1a}$$

$$L_{\text{cen}} = \left\lfloor \left(L_{\text{local}} + 1.5\right)/3 \right\rfloor \times 3 \tag{1b}$$

In Eq. (1a-b), B and L_{local} represent the local latitude and longitude, respectively. And the longitude of the central meridian is denoted by L_{cen}. The azimuth in the G-K framework can be calculated by:

$$\alpha_{\text{grid}} = \alpha_{\text{gyro}} + \Delta - \gamma \tag{2}$$

In Eq. (2), α_{gyro} is the azimuth directly measured by the gyro RTS. Its error will propagate to the grid azimuth α_{grid}, which impacts the measured coordinates of targets eventually. Having been oriented to the grid north, the gyro RTS fits into the auxiliary framework, which is parallel to the grid but takes the RTS as the origin. Then it needs one control point to translate the auxiliary framework to the G-K framework. In regular surveys, the control point is where the station stands. However, things are different on the fully mechanised coal face for two reasons. First, if the gyro RTS is fixed upon the point, it cannot move with the continuously advancing face. So manual operation is still necessary. Second, control points are distributed in roadways, setting up the system there will restrict the field of view to the face.

Mining on a fully mechanised coal face is shown in Fig. 2. The shearer moves along the conveyor, which is connected with hydraulic supports by the oil jacks. The coal face is continuously advancing by the supports pulling and pushing the conveyor. To accord with the mining process, we change the installation and the measuring process of the gyro RTS: it is hung and
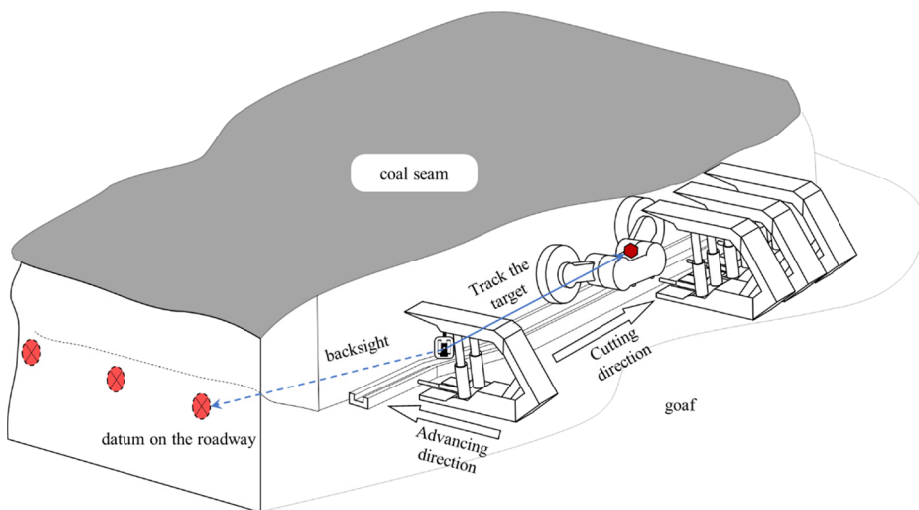
Fig. 2. Main equipment and mining on the fully mechanised coal face

fixed on the hydraulic support, and the control point is regarded as back sight datum (Fig. 2). Compared with the conventional manual operation (Fig. 3), the gyro RTS can work on the newest face after automated quickly levelling and orienting. In this way, not only can it move automatically, but also extend the field of view to the face, helping it search and track the target easier.

Manual Operation	This method
Center the station	Gyro orients itself
Gyro orients itself	Compensate convergence of meridians
Compensate convergence of meridians	Measure one GCP as back sight
Measure the target using the polar method	Measure the target using the polar method
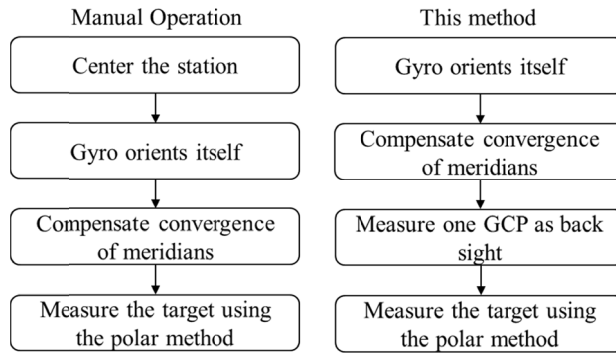
Fig. 3. Comparison of manual operation and automated method

2.2. The state transferring model of the gyro RTS

By analysing the whole work flow of measurement in section 2.1, the automated model can be abstracted into two stages: setting up the station and measuring the specified target. Both stages are elaborated by several specific states of the gyro RTS and their transfers (Fig. 4). The state implies what the gyro RTS is doing now and what it is to do next. Their transfers are driven by so-called events, which are either instructions to the gyro RTS or responses of the RTS to the instructions. By defining the states and their transfers, the complete workflow of automated measuring can be extracted.

In the setting up stage, the gyro RTS is instructed to level itself, orient the coordinate framework, search and then register the relative coordinates of control points. The detailed state transferring in the first stage is as follows. After the gyro RTS levels and orients itself, it is "ready for searching control points". At that point, once the gyro RTS receives the "search" instruction, it will start "searching control points", where its power search and ATR functions play roles. After a while, the gyro RTS returns the search result. If it fails, it will go back to "ready for searching control points". Otherwise, the gyro RTS enters the "control point found" state, to accept or refuse the searched point depending on whether the point is a valid control point. Once accepting the result, the next state will be "registering the control point", namely using the coordinates of the searched control point to translate the framework. Whereas refusing the result makes the state back to "ready for searching control points".

Only when the gyro RTS is set up, can the process enter the measuring stage, where the gyro RTS is instructed to measure the coordinates of a specified target prism. The prism can be attached to the shearer on the fully mechanised coal face. No matter whether the target keeps static or dynamic, the gyro RTS can lock and track it. The state transferring in this stage is similar to that in the setting-up stage. The search procedures are almost identical, except for the criteria for accepting searched results. In this stage, the criterion is whether the searched point is the one

480
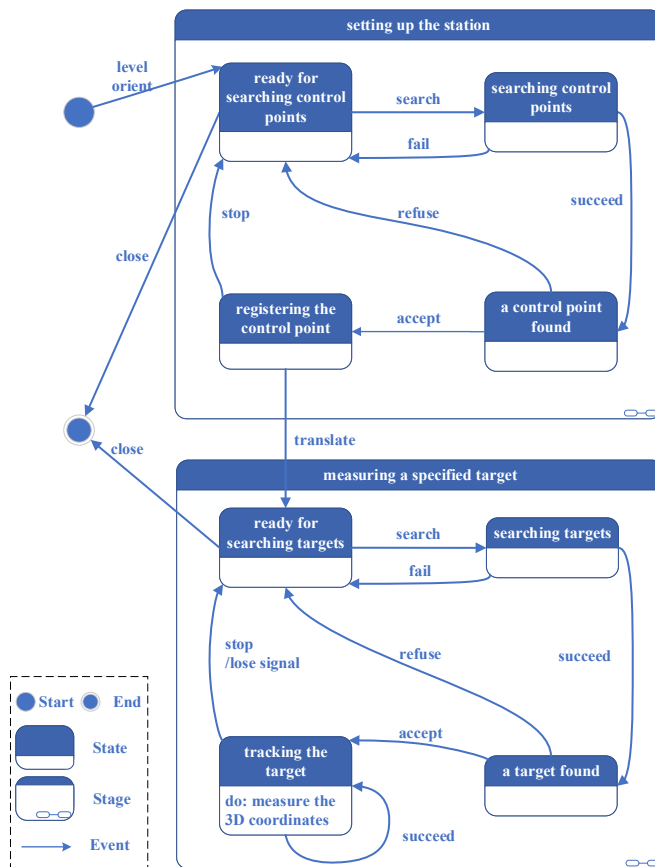
Fig. 4. The state transferring model of measuring

with the specified ID. Whilst in the setting up stage, the searched point will be only accepted if it is a valid control point. After accepting the target, the RTS tightly tracks it and measures its coordinates. The "tracking-measuring" loop will continue until the target is lost or manual interference happens.

2.3. Errors of measured points using the gyro RTS

According to the precision indicators of the gyro RTS, the error of measured coordinates can be derived. As crucial components of gyro RTS, the gyroscope and the RTS determine the accuracy of measured coordinates. The precision of the gyro bias of the gyroscope will affect the azimuth. The precisions of angle measuring and distance measuring of the RTS both affect the azimuth, vertical angle and coordinates. Note that the gyroscope is only related to horizontal measurements and does not interfere with vertical coordinates, so 3D coordinate errors can be divided into vertical and horizontal parts. First, we derive the vertical, and then we consider the horizontal counterpart.
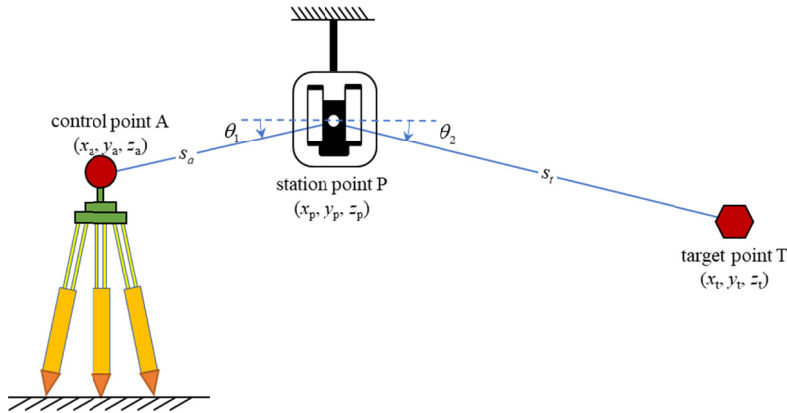
Fig. 5. The trigonometric levelling using RTS

As shown in Fig. 5, the vertical coordinate of the target point is measured by the trigono-metric levelling method. The vertical coordinate of target point T is:

$$z_t = z_p + s_t \sin \theta_2 = z_a - s_a \sin \theta_1 + s_t \sin \theta_2 \tag{3}$$

In Eq. (3), z_a, z_p and z_t denote the vertical coordinate of control point A, station point P and target point T, respectively. θ_1 and s_a denote the vertical angle and slope distance from P to A, while θ_2 and s_t are the counterparts from P to point T. It should be noted that the vertical angle is negative when the RTS looks down, while the value is positive when the RTS looks up. According to the rules for error propagation and Eq. (3), the accuracy indicator of z_t can be derived:

$$\sigma_{z_t}^2 = \sigma_{z_A}^2 + \sigma_{\theta_1}^2 s_a^2 \cos^2 \theta_1 + \sigma_{s_a}^2 \sin^2 \theta_1 + \sigma_{\theta_2}^2 s_t^2 \cos^2 \theta_2 + \sigma_{s_t}^2 \sin^2 \theta_2 \tag{4}$$

In Eq. (4), σ_{zA} and σ_{zt} denote the accuracy of z_A and z_t. $\sigma_{\theta1}$, σ_{sa}, $\sigma_{\theta2}$ and σ_{st} are the counterparts of θ_1, s_a, θ_2 and s_t, respectively, which are commonly given by the instrumental specification.
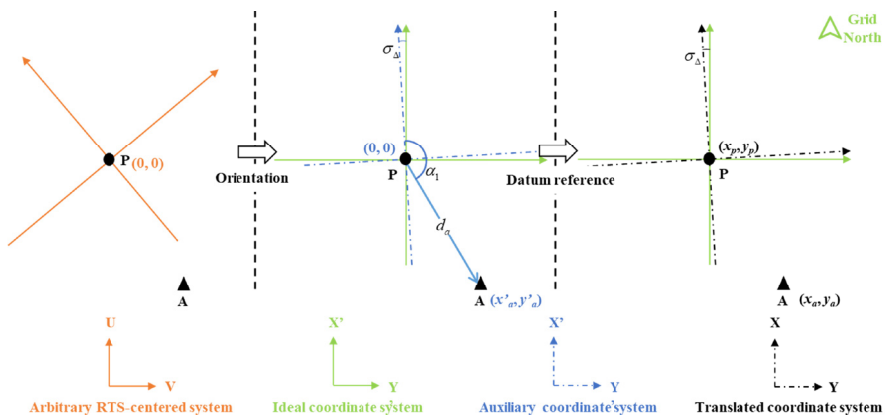
Fig. 6. Setting up the gyro RTS using backsight method

The horizontal errors are derived as follows. As Fig. 6 shows, although the gyro RTS has oriented itself and corrected the bias and the convergence of meridians, the error is still inevitable between the auxiliary coordinate system and the ideal coordinate system, which is denoted as σ_Δ. To translate the auxiliary coordinate system, the RTS measures the horizontal distance and the azimuth to control point A. Then the coordinates of station point P can be obtained.

$$\begin{pmatrix} x_p \\ y_p \end{pmatrix} = \begin{pmatrix} x_a \\ y_a \end{pmatrix} - d_a \begin{pmatrix} \cos\alpha_1 \\ \sin\alpha_1 \end{pmatrix} \tag{5}$$

In Eq. (5), the azimuth α_1 denotes the grid azimuth given by Eq. (2), while d_a is the horizontal component of slope distance s_a in Eq. (3). According to the rules for error propagation, the accuracy of point P is:

$$\begin{pmatrix} \sigma_{x_p}^2 \\ \sigma_{y_p}^2 \end{pmatrix} = \begin{pmatrix} \sigma_{x_A}^2 \\ \sigma_{y_A}^2 \end{pmatrix} + \begin{pmatrix} \cos^2\alpha_1 & d_a^2\sin^2\alpha_1 & d_a^2\sin^2\alpha_1 \\ \sin^2\alpha_1 & d_a^2\cos^2\alpha_1 & d_a^2\cos^2\alpha_1 \end{pmatrix} \begin{pmatrix} \sigma_{d_a}^2 \\ \sigma_\alpha^2 \\ \sigma_\Delta^2 \end{pmatrix} \tag{6}$$

In Eq. (6), σ_{xa} and σ_{ya} denote the horizontal precision of control point A, which are available from the control points report. σ_{da} and σ_α denote accuracy indicators of d_a and angle measuring, respectively. The accuracy indicator of the gyro bias is denoted as σ_Δ. Note that σ_α and σ_Δ are constant indicators of the gyro RTS, but σ_{da} is related to the slope distance s_a and vertical angle θ_1:

$$\sigma_{d_a}^2 = \sigma_{s_a}^2\cos^2\theta_1 + \sigma_{\theta_1}^2 s_a^2\sin^2\theta_1 \tag{7}$$

Symbols in Eq. (7) have the same meanings as those in Eq. (4). Based on the accuracy of point P, we derive the horizontal coordinates of target T and their errors. Using the polar method (Fig. 7), the coordinates of target point T are:

$$\begin{pmatrix} x_t \\ y_t \end{pmatrix} = \begin{pmatrix} x_p \\ y_p \end{pmatrix} + d_t \begin{pmatrix} \cos\alpha_2 \\ \sin\alpha_2 \end{pmatrix} \tag{8}$$
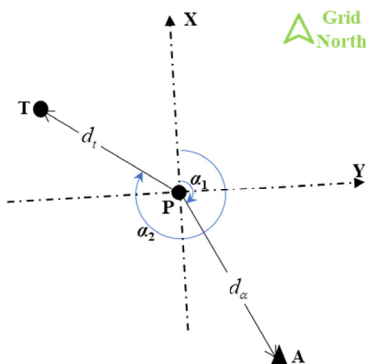
Fig. 7. Measuring target point T using the polar method

In Eq. (8), d_t and α_2 denote the horizontal distance and azimuth from point P to target T. According to the rules for error propagation, the accuracy of horizontal coordinates T is:

$$
\begin{pmatrix} \sigma_{x_t}^2 \\ \sigma_{y_t}^2 \end{pmatrix} = \begin{pmatrix} \sigma_{x_p}^2 \\ \sigma_{y_p}^2 \end{pmatrix} + \begin{pmatrix} \cos^2 \alpha_2 & d_t^2 \sin^2 \alpha_2 & d_t^2 \sin^2 \alpha_2 \\ \sin^2 \alpha_2 & d_t^2 \cos^2 \alpha_2 & d_t^2 \cos^2 \alpha_2 \end{pmatrix} \begin{pmatrix} \sigma_{d_t}^2 \\ \sigma_{\alpha}^2 \\ \sigma_{\Delta}^2 \end{pmatrix}
\tag{9}
$$

In Eq. (9), σ_{xp}, σ_{yp}, σ_{α} and σ_{Δ} keep the same meanings in Eq. (6). σ_{dt} is related to the slope distance s_t and vertical angle θ_2 to point T:

$$
\sigma_{d_t}^2 = \sigma_{s_t}^2 \cos^2 \theta_2 + \sigma_{\theta_2}^2 s_t^2 \sin^2 \theta_2
\tag{10}
$$

Bringing the results of Eq. (6), (7) and (10) to Eq. (9), the horizontal coordinates errors of target T can be estimated:

$$
\begin{pmatrix} \sigma_{x_t}^2 \\ \sigma_{y_t}^2 \end{pmatrix} = \begin{pmatrix} \sigma_{x_A}^2 \\ \sigma_{y_A}^2 \end{pmatrix} + \begin{pmatrix} \cos^2 \alpha_1 & \cos^2 \alpha_2 \\ \sin^2 \alpha_1 & \sin^2 \alpha_2 \end{pmatrix} \begin{pmatrix} \sigma_{d_a}^2 \\ \sigma_{d_t}^2 \end{pmatrix}
$$
$$
+ \begin{pmatrix} d_a^2 \sin^2 \alpha_1 + d_t^2 \sin^2 \alpha_2 & d_a^2 \sin^2 \alpha_1 + d_t^2 \sin^2 \alpha_2 \\ d_a^2 \cos^2 \alpha_1 + d_t^2 \cos^2 \alpha_2 & d_a^2 \cos^2 \alpha_1 + d_t^2 \cos^2 \alpha_2 \end{pmatrix} \begin{pmatrix} \sigma_{\alpha}^2 \\ \sigma_{\Delta}^2 \end{pmatrix}
\tag{11}
$$

3. The Prototype System

To justify the automated measuring model, programs were developed and installed on available instruments forming the prototype. The prototype and the model have been published as patents already [29-31].

3.1. System Framework

System functions include automatically measuring the target and outputting its real-time coordinates. After the system is started, except for special circumstances such as hardware abnormalities, it can achieve levelling, orientation, tracking and measuring the target on its own. The geodetic coordinates are required to be transmitted in real-time to the server. System inputs include the approximate search angle of control points and targets and the latitude and longitude of the working face. And outputs include system current information and the real-time 3D geodetic coordinates of the target.

3.2. Hardware

The hardware composition mainly includes a gyro RTS, an industrial personal computer (IPC), and a remote computer. The gyro RTS and the industrial computer are connected via wires through a series of ports, allowing them to communicate with each other. The remote computer and the

484

IPC communicate with each other through the Intranet. To accord with the safety requirements in underground coal mines, an explosion-proof shell is installed on the device (Fig. 8). The nominal accuracy of the gyroscope is 90", and the RTS's accuracy specifications are shown in TABLE 1.

TABLE 1

Accuracy specifications of the RTS *

Measurement	Mode	Value
Angle	continuously	0.5"
Distance	Single (prism)	0.6 mm + 1 ppm
	Single (any surface)	2 mm + 2 ppm

* Temperature: –20°C to +50°C Humidity: 95% non-condensing Environment: overcast, no haze, visibility about 40 km, no heat shimmer
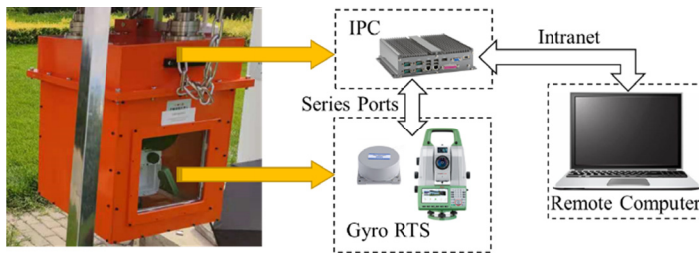
Fig. 8. The hardware components of the automated gyro RTS system

3.3. Software

The software composition mainly includes an operator program, a controller program and related communication protocols (Fig. 9). The operator program is deployed in the IPC, sending control instructions to the gyro RTS and sending system information to the controller program. The controller program is deployed in the remote computer, sending instructions to the operator program and receiving corresponding feedback. The state-transferring model is the basis of the controller program. Last but not least, related protocols play roles in message communication. The GeoCOM protocol works between the gyro RTS and the operator program, while the custom protocol works between the operator program and the controller program.

The controller program is the core of the software part, which is developed based on the "Model-View-Control" concept and multi-threading technology (Fig. 10). The basic "model"
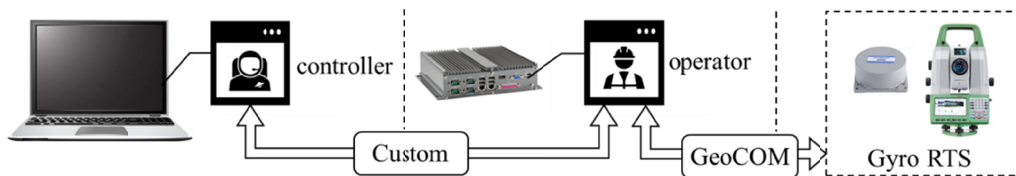
Fig. 9. The software components of the gyro RTS automated system

is the *Node*, which derives the *Point* and the *Gyro RTS Server*. The *Gyro RTS Server* implements the state-transferring model by defining the *State* and handling real-time messages. The *Node Manager* acts as the "controller" and is used to maintain gyro total stations, control points and targets. The "view" is realised using the observer mode, where the *Node* can remind the *Node Manager*, to update the user interface to the current status. Multiple threads work simultaneously in connecting to the RTS client, monitoring and transferring the states of the RTS. The user interface is used to read configuration files and display system information. Results are published by message queues and stored in databases.
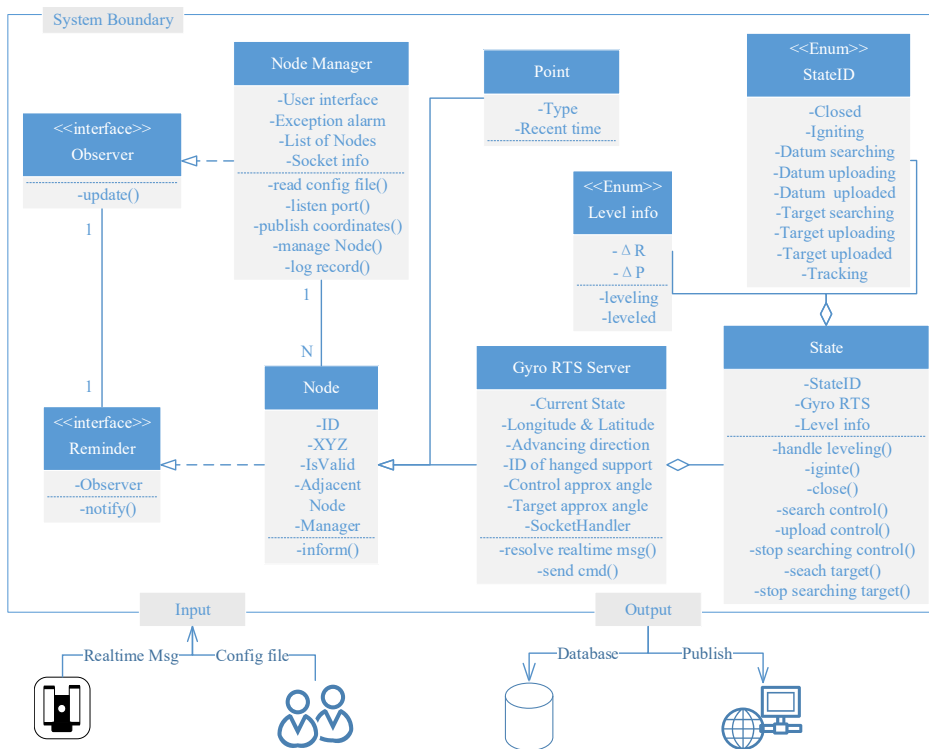
Fig. 10. Object-oriented design of controller program

4. Experiments and Results

Field experiments were conducted on a simulative working face to evaluate the measuring accuracy and applicability of the prototype.

4.1. Environment and settings

The simulative working face includes the conveyor, the shearer and the supports (Fig. 11). It is noted that the setting of the experiments (Fig. 12). The gyro RTS hangs on the hydraulic

486

support, equipped with an ad-hoc levelling device, which can automatically adjust the length of three pillars to keep the system still and levelled. The setting of experiments stimulated the working scenarios on the underground fully mechanised face, which moves the prototype along with the hydraulic support and saves manual operations.

Fig. 11. Simulative working face on the ground

hydraulic support

leveling device
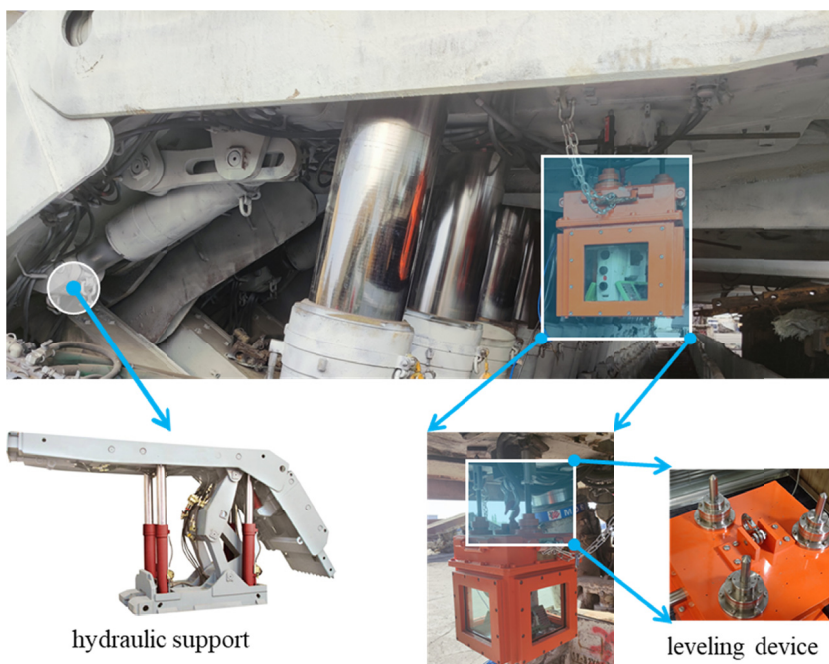
Fig. 12. Setting the system in field experiments

The GNSS method was used to obtain geodetic coordinates for various points, which was compared with measured results to calculate the errors. The distribution of reference points can be seen in Fig. 13.
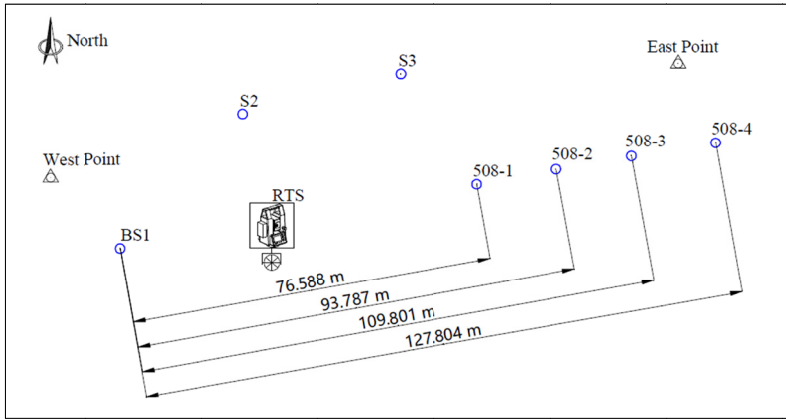
Fig. 13. Distribution of reference points on the test field

4.2. Results

Point BS1 was regarded as the roadway datum, whilst points 508-1, 508-2, 508-3 and 508-4 were regarded as shearer targets. Using the prototype measuring targets with 3 Hz sampling rate and keeping around 10 minutes, the errors between measured values and ground truth values are shown in Fig. 14.
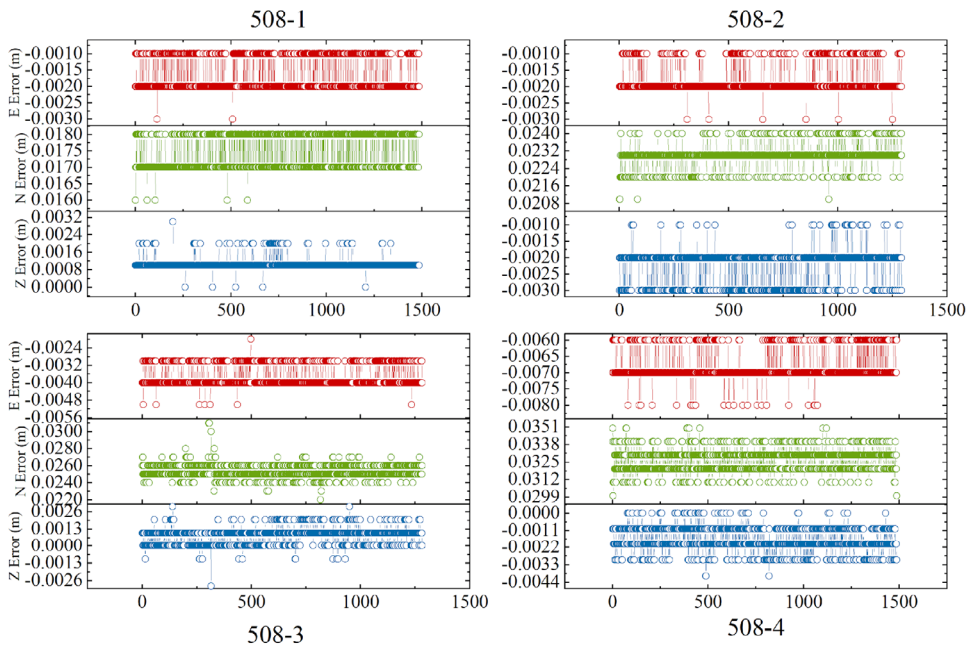
Fig. 14. The spatiotemporal distribution of coordinates error of 508-1, 508-2, 508-3 and 508-4

As shown in Fig. 14, on each target, there are about 1500 successive records collected. Because the coordinate resolution of the RTS is one millimetre, errors in single dimensions are distributed repeatedly at few values on vertical axes. The extreme values of errors in the same single dimension differ by only millimetres, which means the measurements are internally stable. The measurements have biases to ground relatively notable truths with errors at the centimetre level.
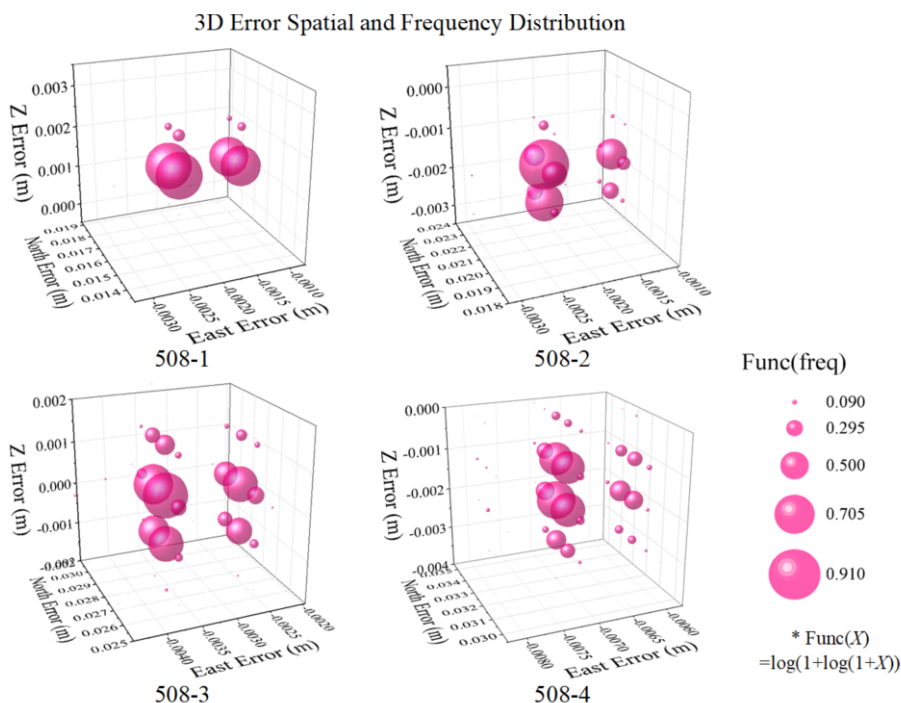
Fig. 15. The 3D distribution of targets

By counting up their frequencies, the frequency distribution of errors can be obtained (Fig. 15). Note that we used $\text{Func}(X) = \log(1 + \log(1 + X))$ to visualise the frequency of 3D errors, to shrink the differences between their original frequencies. When using the original values, the extreme differences are too significant to be displayed effectively. This results in the smallest value being barely visible or the largest value being unable to fit in the graph. From 508-1 to 508-4, the 3D scatters are increasingly dispersive with larger distances, implying that the accuracy is decreasing. To quantify the measurement error, we calculated the root mean square error (RMSE) of points. The RMSE is convenient to estimate the accuracy of coordinates because it describes both the deviation of the variable and its bias against the ground truth. Moreover, based on the distances, we can calculate the relative RMSE. The RMSE is calculated by Eq. (21):

$$RMSE(T) = \sqrt{\frac{1}{n}\sum_{i=1}^{n} error^2(T_i)} \tag{21}$$

In Eq. (21), $error(T_i)$ denotes the coordinates error of target T, and it is calculated by Eq. (22):

$$error(T) = \sqrt{\left(x_T - \tilde{x}_T\right)^2 + \left(y_T - \tilde{y}_T\right)^2 + \left(z_T - \tilde{z}_T\right)^2} \qquad (22)$$

In Eq. (22), $(\tilde{x}_T, \tilde{y}_T, \tilde{z}_T)$ are the ground truth coordinates of point T and (x_T, y_T, z_T) are its measured coordinates. The RMSE results are shown in TABLE 2.

TABLE 2

Distances from BS1 to targets and RMSEs (three components and the total)

Target ID	Distance from BS1 (m)	RMSE (cm)				3D Relative RMSE (10^{-4})
		East	North	Z	3D	
508-1	76.588	0.1672	1.7499	0.1077	1.7612	2.2996
508-2	93.783	0.1843	2.2984	0.2317	2.3174	2.4710
508-3	109.801	0.3700	2.5341	0.1006	2.5630	2.3342
508-4	127.804	0.6824	3.2655	0.1857	3.3412	2.6143

From 508-1 to 508-4, the horizontal RMSEs (i.e. the east and the north direction) increase notably, while the vertical RMSEs (i.e. the Z direction) are relatively smaller and seem to distribute randomly. Affected by the horizontal component, the RMSE of 3D errors are at the centimetre level and increase with larger distances. But the relative RMSEs appear to have no obvious tendency, and the maximum is only 2.6143×10^{-4}.

5. Discussion

Based on the results in Table 2, horizontal errors and vertical errors differ significantly. The former are in centimetre level and increase with larger distance, while the latter are in millimetre level and change randomly. Note that the impact factors between vertical and horizontal coordinates are different (derived by Eq. (4) and Eq. (6), respectively). Vertical errors are caused only by the total station's range and angle measurements, while horizontal errors are affected by the gyroscope. According to the millimetre level precision and the randomness of vertical errors, the total station appears to be precise and stable. Therefore, the major source of horizontal errors probably results from the gyroscope. We then investigated the accuracy of the gyroscope.

Because the gyroscope only influences horizontal zero direction, and azimuths measuring eastern and northern errors are focused. The characteristics of horizontal errors can be investigated by their covariance matrices and error ellipses. First of all, the covariance matrix of horizontal coordinates is calculated by:

$$\mathbf{Cov}\left(\begin{bmatrix} x \\ y \end{bmatrix}\right) = \begin{bmatrix} Q_{xx} & Q_{xy} \\ Q_{yx} & Q_{yy} \end{bmatrix} = \frac{\sum_{i=1}^{n} \begin{bmatrix} x_i - \tilde{x} \\ y_i - \tilde{y} \end{bmatrix} \begin{bmatrix} x_i - \tilde{x} & y_i - \tilde{y} \end{bmatrix}}{n} \qquad (23)$$

In Eq. (23), Q_{xx} and Q_{yy} denote the north and east coordinates variances from ground truths. Q_{xy} denotes the covariance of north and east coordinates. And then, the error ellipse can be derived from the elements of the covariance matrix:

490

$$K = \sqrt{\left(Q_{xx} - Q_{yy}\right)^2 + 4Q_{xy}^2} \qquad (24a)$$

$$E^2 = \frac{1}{2}\left(Q_{xx} + Q_{yy} + K\right) \qquad (24b)$$

$$F^2 = \frac{1}{2}\left(Q_{xx} + Q_{yy} - K\right) \qquad (24c)$$

$$\tan 2\varphi = \frac{2Q_{xy}}{Q_{xx} - Q_{yy}} \qquad (24d)$$

In Eq. (24), E and F are the lengths of the major and minor axis of the ellipse, respectively. φ denotes the direction of the major or the minor axis. Calculated results are shown in TABLE 3 and Fig. 16. It is interesting to find that the four error ellipses are all flat and all orient to the centroids of samples from the ground truths (denoted by the arrows). The flat shapes imply the error disparity in the major and minor directions, and the directions of ellipses imply similar azimuth biases. In addition, from 508-1 to 508-4, the size of ellipses grows with larger distances, in accord with the RMSEs in TABLE 2.

TABLE 3

Parameters of error ellipses

Target ID	Parameters		
	E (m)	F (m)	φ (rad)
508-1	0.01757	0.0004934	–0.08945
508-2	0.02305	0.0004115	–0.07703
508-3	0.02561	0.0004693	–0.1382
508-4	0.03440	0.0004474	–0.2689

The increasing lengths of ellipse major axes imply the increasing errors caused by the azimuth bias. The horizontal errors grow with larger distances. According to the distances from BS1 to each target, the error of gyro (i.e. Δ in Eq. (2)) can be estimated:

TABLE 4

Errors of gyro

E (m)	Distance from BS1 (m)	Errors (")
0.01757	76.588	47.3191
0.02305	93.783	50.6958
0.02561	109.801	48.1092
0.03440	127.804	55.5187

TABLE 4 shows the maximum estimated error of gyro is 55.5187", below the nominal indicator of 90". Moreover, considering that the millimetre level of RTS errors is acceptable, the whole measuring process is performed normally, and the prototype does not influence the original
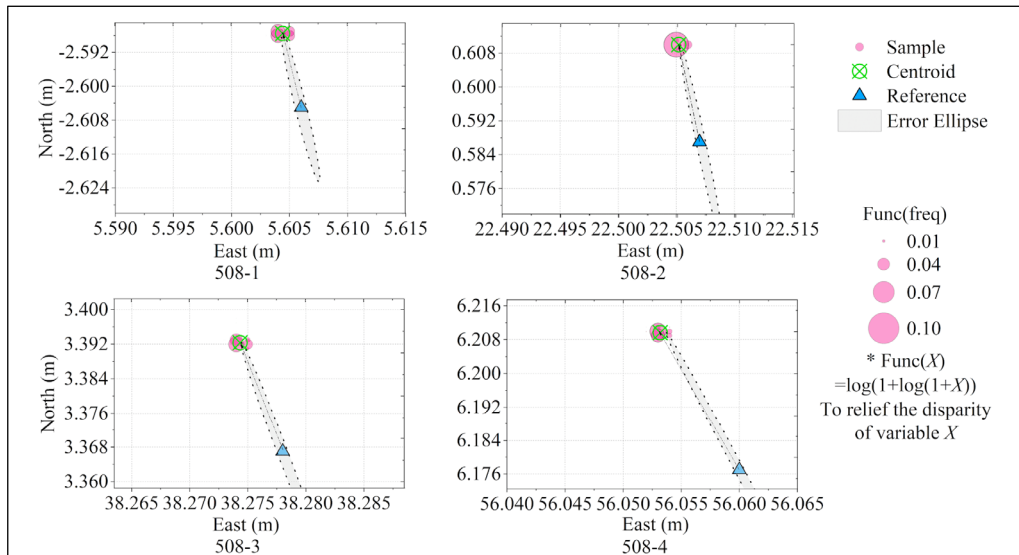
Fig. 16. The error ellipses of horizontal coordinates of four targets

hardware precision. Therefore, the results of field experiments imply the good performance and applicability of the proposed system.

6. Conclusions

Aiming to solve the problems (e.g. low accuracy, low automation, low applicability) of positioning equipment on advancing fully mechanised coal faces, this paper proposed an automated gyro RTS measuring system. The system is capable of measuring and transmitting the real-time accurate absolute positions of equipment on the mining face. The research includes 4 highlights as follows:

1. To accord with the working situation on dynamic coal faces, the measuring process of the gyro RTS was changed, and a state transferring model was established, driving the system to track the target and measure its coordinates automatically to replace manual operation.
2. Based on the theoretical model, programs were developed and installed in available instruments, forming a prototype.
3. To verify the accuracy and applicability of the prototype, theoretical error evaluation and field tests were both carried out. Results showed that the relative error of points was better than 2.6143×10^{-4}, which meets the demand of positioning on advancing faces.
4. By analysing the characteristics of coordinates errors, we attributed the major positioning error to the gyroscope. The errors were presented by the error ellipses and estimated at 55.5187", which justifies the gyroscope nominal indicator 90".

On the underground coal mining faces, the proposed automated gyro RTS system can replace manual measurement work. Not only will it decrease the risks to workers, but also provide

accurate and real-time geodetic coordinates of large equipment. It can be used to calibrate INS conveniently. By capturing the reliable positions of equipment, the mining progress can be combined with the geological model, which is conducive to realising adaptive mining and establishing intelligent coal faces.

Acknowledgement

Reference

[1] S.S. Peng, F. Du, J. Cheng, Y. Li, Automation in U.S. longwall coal mining: A state-of-the-art review. International Journal of Mining Science and Technology **29** (2), 151-159 (2019). DOI: https://doi.org/10.1016/j.ijmst.2019.01.005

[2] G. Wang, Y. Xu, H. Ren, Intelligent and ecological coal mining as well as clean utilisation technology in China: Review and prospects. International Journal of Mining Science and Technology **29** (2), 161-169 (2019). DOI: https://doi.org/10.1016/j.ijmst.2018.06.005

[3] W. Song, J. Cheng, W. Wang, Y. Qin, Z. Wang, M. Borowski, P. Tukkaraja, Underground Mine Gas Explosion Accidents and Prevention Techniques – An overview. Archives of Mining Sciences **66** (2), 297-312 (2021). DOI: https://doi.org/10.24425/ams.2021.137463

[4] J. Wang, M. Jia, L. Bin, L. Wang, D. Zhong, Regulation and Optimization of Air Quantity in a Mine Ventilation Network with Multiple Fans. Archives of Mining Sciences **67** (1), 179-193 (2022). DOI: https://doi.org/10.24425/ams.2022.140709

[5] S. Şalap, M. O. Karslıoğlu, N. Demirel, Development of a GIS-based monitoring and management system for underground coal mining safety. International Journal Of Coal Geology **80** (2), 105-112 (2009). DOI: https://doi.org/10.1016/j.coal.2009.08.008

[6] G. Wang, G. Zhao, H. Ren, Analysis on key technologies of intelligent coal mines and intelligent mining. Meitan Xuebao/Journal of the China Coal Society **44** (1), 34-41 (2019). DOI: https://doi.org/10.13225/j.cnki.jccs.2018.5034

[7] S. Mao, J. Cui, S. Wang, X. Tu, P. Zhang, M. Li, Construction of an information sharing platform of mine safe production for intelligent mining. Meitan Xuebao/Journal of the China Coal Society **45** (6), 1937-1948 (2020). DOI: https://doi.org/10.13225/j.cnki.jccs.ZN20.0341

[8] M. Van Dyke, T. Klemetti, J. Wickline, Geologic data collection and assessment techniques in coal mining for ground control. International Journal of Mining Science and Technology **30** (1), 131-139 (2020). DOI: https://doi.org/10.1016/j.ijmst.2019.12.003

[9] D.C. Reid, D.W. Hainsworth, J.C. Ralston, R.J. McPhee, Shearer guidance: A major advance in longwall mining. In: S. Yuta , H. Asama (Eds), Field and Service Robotics. Springer Tracts in Advanced Robotics **24**. Springer, Berlin, Heidelberg 2006.

[10] A. Yassin, Y. Nasser, M. Awad, A. Al-Dubai, R. Liu, C. Yuen, R. Raulefs, E. Aboutanios, Recent Advances in Indoor Localization: A Survey on Theoretical Approaches and Applications. IEEE Communications surveys and tutorials **19** (2), 1327-1346 (2017). DOI: https://doi.org/10.1109/COMST.2016.2632427

[11] N. Wang, X. L. Shen, Research on WSN nodes location technology in coal mine. In: Q. Zhou(Eds.), IFCSTA 2009 Proceedings - 2009 International Forum on Computer Science-Technology and Applications, IEEE 2009.

[12] B. Srikanth, H. Kumar, K.U.M. Rao, A robust approach for WSN localization for underground coal mine monitoring using improved RSSI technique. Mathematical Modelling of Engineering Problems **5** (3), 225-231 (2018). DOI: https://doi.org/10.18280/mmep.050314

[13] F. Evennou, F. Marx, Advanced Integration of WiFi and Inertial Navigation Systems for Indoor Mobile Positioning. EURASIP Journal on Advances in Signal Processing 2006 (1), 086706 (2006). DOI: https://doi.org/10.1155/ASP/2006/86706

[14] C.O. Hargrave, C.A. James, J.C. Ralston. Infrastructure-based localisation of automated coal mining equipment. International Journal of Coal Science & Technology **4** (3), 252-261 (2017). DOI: https://doi.org/10.1007/s40789-017-0180-3

[15] S. Huh, U. Lee, H. Shim, J.-B. Park, J.-H. Noh, Development of an unmanned coal mining robot and a tele-operation system.In: 2011 11th International Conference on Control, Automation and Systems, IEEE 2011.

[16] X. Yang, X. Yu, C. Zhang, S. Li, Q. Niu, MineGPS: Battery-free Localization Base Station for Coal Mine Environment. IEEE communications letters:1-1. (2021). DOI: https://doi.org/10.1109/LCOMM.2021.3081593

[17] J. Zheng, S. Li, N. Li, Q. Fu, S. Liu, G. Yan, A LiDAR-Aided Inertial Positioning Approach for a Longwall Shearer in Underground Coal Mining. Mathematical Problems in Engineering 2021, 6616090 (2021). DOI: https://doi.org/10.1155/2021/6616090

[18] J. Xu, E. Wang, R. Zhou, Real-time measuring and warning of surrounding rock dynamic deformation and failure in deep roadway based on machine vision method. Measurement **149**, 107028 (2020). DOI: https://doi.org/10.1016/j.measurement.2019.107028

[19] J. Zhou, H. Xiao, W. Jiang, W. Bai, G. Liu, Automatic subway tunnel displacement monitoring using robotic total stations. Measurement, Journal of the International Measurement Confederation **151**,107251 (2020). DOI: https://doi.org/10.1016/j.measurement.2019.107251

[20] B. Liu, Y. Wei, Optimization of Location of Robotic Total Station in Tunnel Deformation Monitoring. In: W. Wu, H. Yu (Eds.), Proceedings of China-Europe Conference on Geotechnical Engineering, Cham: Springer International Publishing 2018.

[21] J. Zhou, B. Shi, G. Liu, S. Ju, Accuracy analysis of dam deformation monitoring and correction of refraction with robotic total station. PLoS One **16**(5) (2021). DOI: http://dx.doi.org/10.1371/journal.pone.0251281

[22] J. Yu, P. Zhu, B. Xu, X. Meng, Experimental assessment of high sampling-rate robotic total station for monitoring bridge dynamic responses. Measurement **104**, 60-69 (2017). DOI: https://doi.org/10.1016/j.measurement.2017.03.014

[23] P.A. Psimoulis, S.C. Stiros, Measuring deflections of a short-span railway bridge using a robotic total station. Journal of Bridge Engineering **18**(2),182-185 (2013). DOI: https://10.1061/(ASCE)BE.1943-5592.0000334

[24] Z.G. Xia, C. Zhang, Y. Zheng, L.X. Jiang, An astronomical azimuth measurement system aided with an automatic gyro total station. In: K. Fan (Eds.), 3rd International Symposium on Precision Mechanical Measurements; 2006 Aug 02-06; Urumqi, Peoples r China. BELLINGHAM: Spie-Int Soc Optical Engineering 2006.

[25] Y. Yu, Z. Men, The baseline field establishes an instrument constant measuring of gyro total station. Engineering of Surveying and Mapping **24** (12), 72 (2015).

[26] T. Wang, H.R. Duan, L.T. Jiang, S. Liu, Analysis of Underground Space Azimuth Measuring and Data Processing in A Tunnel. In: C. Chen (Eds.), 4th International Conference on Civil Engineering, Architecture and Building Materials (CEABM); 2014 May 24-25; Haikou, Peoples R China. DURNTEN-ZURICH: Trans Tech Publications Ltd 2014.

[27] P.P. Bahuguna, Correlation survey for shaft deepening in Digwadih underground coal mine. J. Surv. Eng.-ASCE **129** (1), 33-36 (2003). DOI: https://doi.org/10.1061/(asce)0733-9453(2003)129:1(33)

[28] X. Zhang, W. Liu, F. Xie, L. Shi, Application research on some problems of mine connection measurement. Engineering of Surveying and Mapping **29** (6), 44 (2020).

[29] S. Mao, X. Zhang, X. Li, Y. Tai, H. Chen, J. Liu, inventor; Beijing Longruan Technologies INC. & Tianjin Navigation Instruments Research Institute,assignee. Measuring-robot device for fully mechanised coal mining face and automatic measuring system. Chinese patent: CN112378390B,2021.05.25.

[30] S. Mao, X. Zhang, X. Li, Y. Tai, H. Chen, J. Liu, inventor; Beijing Longruan Technologies INC. & Tianjin Navigation Instruments Research Institute,assignee. Measuring-robot device for fully mechanised coal mining face and automatic measuring system. Canada Patent: CA3144609A, 2022.04.19.

[31] S. Mao, X. Zhang, X. Li, Y. Tai, H. Chen, J. Liu, inventor; Beijing Longruan Technologies INC. & Tianjin Navigation Instruments Research Institute,assignee. Measuring-robot device for fully mechanised coal mining face and automatic measuring system. United States patent: US20220221276A1, 2022.07.14.